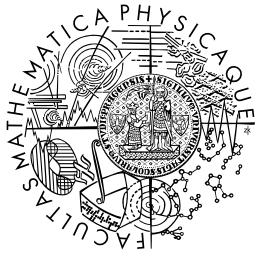

FACULTY
OF MATHEMATICS
AND PHYSICS
Charles University

BACHELOR THESIS

Ondřej Knopp

Electrical conductivity of the mantle and its thermochemical and mineralogical state: Forward problem

Department of Geophysics

Supervisor of the bachelor thesis: Jakub Velímský
Study programme: Physics (FOF)
Study branch: Physics

Prague 2021

I declare that I carried out this bachelor thesis independently, and only with the cited sources, literature and other professional sources. It has not been used to obtain another or the same degree.

I understand that my work relates to the rights and obligations under the Act No. 121/2000 Sb., the Copyright Act, as amended, in particular the fact that the Charles University has the right to conclude a license agreement on the use of this work as a school work pursuant to Section 60 subsection 1 of the Copyright Act.

In ..... date ....

Author's signature

This research was funded by the Grant Agency of the Czech Republic, project No. 20-07378S, and the Swarm DISC activities, ESA contract No. 4000109587.

Title: Electrical conductivity of the mantle
and its thermochemical
and mineralogical state:
Forward problem

Author: Ondřej Knopp

Department: Department of Geophysics

Supervisor: Jakub Velímský, Department of Geophysics

Abstract: With the increased availability of new geomagnetic data, mainly from the Swarm mission satellites, it is possible to obtain global mantle conductivity models. A subsequent task is to interpret such models in terms of the thermal and chemical structure of the Earth's mantle. It can be done using the experimental conductivity data for major mantle minerals combined with the Gibbs energy minimization. Here I describe these methods and present a forward problem calculating the electrical conductivity of the Earth's mantle, from its temperature and chemical composition. I also present the modelling results for a-priori temperature and compositional settings. This software component will become part of the existing tools used for global inversion of electromagnetic data to constrain the thermochemical and mineralogical structure of the mantle.

Keywords: Gibbs energy minimalization, mantle composition, electrical conductivity

Contents

Introduction

The Earth's mantle is the subject of long-term ongoing geophysical studies. The material properties of the mantle, such as the P and S seismic wave velocities, the electrical and thermal conductivities, the viscosity and the density are constrained by the seismic, electromagnetic (EM), thermal and gravitational data observed on the Earth's surface or above it. All of the material variables are interlinked by the thermal, chemical and mineralogical state of the mantle.

The distribution of the mantle electrical conductivity, which can not be measured *in situ*, is studied indirectly by the means of the electromagnetic induction methods. On the planetary scale, the main sources of the EM energy interacting with the mantle are the electric currents in the magnetosphere, the ionosphere, and the currents induced motionally in the Earth's oceans by tidal flows. Recently, the Swarm multi-satellite mission of the European Space Agency, the expanding network of the ground geomagnetic observatories, and the advances of modern EM forward and inverse modelling have enabled an unprecedently detailed view of the electrical conductivity structure of the mantle. An overview of recent advances in this area is presented by (Kuvshinov, 2015). More recently, Grayver et al. (2017) have combined the EM induction by the tidal and magnetospheric sources to constrain the electrical conductivity of the oceanic upper mantle and the transition zone. Fully three-dimensional (3-D) inversion of Swarm satelite data in terms of mid-mantle electrical conductivity distribution has been recently carried out by Velímský and Knopp (2021) and Kuvshinov et al. (2021).

The link between the material variables and the thermal, chemical and mineralogical state of the mantle can be explained with the thermochemical modelling (Connolly, 1990, 2005, 2009). Whereas most of the material properties are a direct product of this method, the electrical conductivity has to be coupled with the experimental high-pressure measurements. This approach is illustrated by a review of Khan (2016). For one-dimensional (1-D) inversion of the observatory-based EM data he obtained the chemical and thermal structure of the upper mantle and transition zone. Recently (Martinec et al., 2021), this approach was used for construction of a 3-D conductivity model of the upper mantle from a thermal and compositional model WINTERC-G, created by inverting the seismic, gravity and heat-flow data (Fullea et al., 2021).

The goal of this thesis is to develop a modular code for calculation of the mantle electrical conductivity from its thermal and compositional state, suitable for a future merge with the forward and inverse EM induction modelling codebase developed at the Charles University (e.g., Velímský and Martinec, 2005; Velímský, 2013; Velímský et al., 2018; Velímský and Knopp, 2021; Šachl et al., submitted). For this purpose I reimplement the experimental-based conductivity database presented by Khan (2016) and couple it with the thermochemical modelling code Perple_X (Connolly, 2009).

1. Forward problem

Purpose of the forward problem is to obtain point-wise values of mantle electrical conductivity for given temperature, pressure, chemical composition and water content. I use the method developed by Khan (2016), which employs thermodynamic modelling approach of Connolly (1990, 2005, 2009).

The forward problem consists of several steps as described by the Figure 1.1. The first step employs Gibbs energy minimization to construct the phase structure of the mantle, which in turn depends on the temperature T, pressure P and chemical composition $\mathbf{X}$. Perple_X, a set of FORTRAN 77 programs for calculating and displaying phase diagrams was created by Connolly (2009). In Chapter 2 I summarize the Gibbs energy minimization approach used in Perple_X for a particular mantle composition with the help of thermodynamic databases constructed by Stixrude and Lithgow-Bertelloni (2005a,b).

The Chapter 3 introduces three charge transport mechanisms present in the silicate mantle. It further presents an overview of the experimental rock conductivities, their dependence on the temperature, the pressure, the water content C_w, and on the phase structure ψ obtained in the previous step. Finally I discuss the problem of averaging the conductivities of individual phases σ_e into the bulk conductivity σ.

In the last chapter I show several examples of depth-conductivity models constructed for geophysically relevant $(T, P, C_w, \mathbf{X})$ conditions. These ad-hoc models are compared with conductivity profiles retrieved form inversions of EM data.

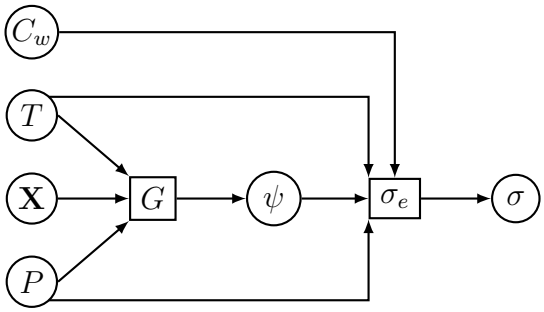

Figure 1.1: The working scheme of the point-wise forward problem. For given temperature T, chemical composition $\mathbf{X}$, and pressure P the minimization of Gibbs energy G provides the phase structure ψ. Combined with the experimental conductivities of individual phases σ_e, and taking into account the water content C_w, temperature T, and pressure P the forward problem finally yields the bulk conductivity σ.

2. Thermochemical modelling

2.1 Gibbs energy minimalization

In this chapter I present the basics of Gibbs energy minimization, and its discretization as implemented in the Perple_X software. I use the formalism and the approach presented in Connolly (1990, 2005, 2009) with some minor changes to the notation.

For a time-independent model of the Earth's mantle, it is possible to characterize a small enough region of the mantle only by its chemical composition, pressure and temperature. In order to determine other physical properties such as density, viscosity, thermal and electrical conductivity, heat capacity and microscopic arrangement of its components, it is sufficient to apply the Gibbs energy minimization approach. The Gibbs energy $G(P, T, \mathbf{X})$ in thermodynamic sense depends only on the temperature T, the pressure P, and the composition vector $\mathbf{X} = (X_1, X_2, \ldots, X_d)$. The composition vector consists of the individual component fractions in the mixture with d components,

$$X_i = N_i/N, \tag{2.1}$$

where N_i is the number of particles of the i-th component, and

$$N = \sum_{i=1}^{d} N_i. \tag{2.2}$$

Obviously, $\mathbf{X}$ lives in the unit d-simplex

$$P_d = \left\{ \mathbf{X} \in [0,1]^d, \sum_{i=1}^{d} X_i = 1 \right\}. \tag{2.3}$$

For fixed (P, T) conditions and a given total chemical composition, $\mathbf{X}^0$, the system can contain up to s coexisting phases in a thermodynamic equilibrium. Each of these phases has a distinct composition vector $\mathbf{X}^j$ and corresponding molar concentration in the system ψ^j. It must hold, that

$$1 = \sum_{j=1}^{s} \psi^j, \tag{2.4}$$

$$\mathbf{X}^0 = \sum_{j=1}^{s} \psi^j \mathbf{X}^j. \tag{2.5}$$

The complete knowledge of the Gibbs energy $G_{P,T}(\mathbf{X}) \equiv G(P, T, \mathbf{X})$ yields the number of phases s, the concentrations ψ^j, and the compositions $\mathbf{X}^j$ of the coexisting phases by minimizing the function

$$g\left(s, \{\psi^j, \mathbf{X}^j\}_{j=1}^{s}\right) = \sum_{j=1}^{s} \psi^j G_{P,T}(\mathbf{X}^j), \tag{2.6}$$

subject to constraints (2.4, 2.5). It can be shown, that the optimal value of this sum lies on the convex hull of the function $G_{P,T}(\mathbf{X})$, where the total composition

vector $\mathbf{X}^0$ is projected on the convex hull as shown in the Figure 2.1. In other words,

$$\sum_{j=1}^{s} \psi^j G_{P,T}(\mathbf{X}^j) \leq G_{P,T}(\mathbf{X}^0). \tag{2.7}$$

Furthermore, the composition vectors of the coexisting phases can be found at the intersections of the function $G_{P,T}(\mathbf{X})$ with its own convex hull. Then the concentrations ψ^j can be viewed as barycentric coordinates of the point $(g, \mathbf{X}^0)$ in a s-simplex with the vertices $\{(G_{P,T}(\mathbf{X}^j), \mathbf{X}^j)\}_{j=1}^{s}$.

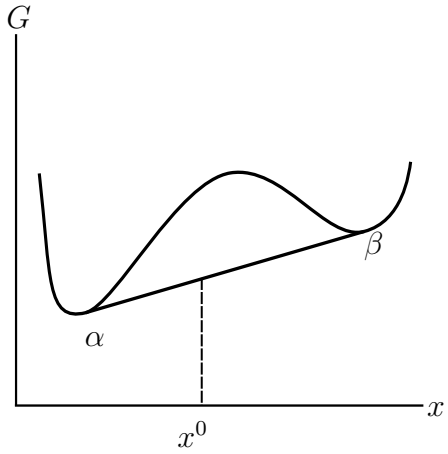

Figure 2.1: A simplified scheme of a two-phase, two-component system $\mathbf{X} = (x, 1-x)$. For a fixed temperature and pressure, there are two minima of the Gibbs energy $G_{PT}(\mathbf{X})$ representing the two phases α and β. For a fixed composition $\mathbf{X}^0 = (x^0, 1-x^0)$, the Gibbs energy $G_{P,T}(\mathbf{X}^0)$ is not optimal. Considering presence of heterogeneities in the system, the optimal Gibbs energy lies on the convex hull of the function $G_{P,T}(\mathbf{X})$.

The number s itself can be determined according to the Gibbs phase rule. It states, that $s = d + 2 - f$, where f is the number of degrees of freedom on the (P, T) phase diagram. For most (P, T) conditions it holds, that $f = 2$. However, when phase transitions occur due to the temperature or the pressure change, the number of degrees of freedom can also reach the value 0 or 1.

Note that s is the maximal number of coexisting phases. For example, if $\mathbf{X}^j = \mathbf{X}^0$ for a particular phase j, then $\psi^j = 1$ and $\psi^i = 0$, $\forall i \neq j$. This concept is generalized also for those $\mathbf{X}^0$ positioned on edges or faces of the s-simplex considered above.

This exact analytical approach has its obvious downsides. First, one has to know the complete function $G(P, T, \mathbf{X})$ in order to construct its convex hull for each P and T. Another complication arises from the identification of the intersection points. Nevertheless, this framework provides an efficient tool to explain the presence of different phases and their coexistence. It also serves as a guide for construction of discrete phase transition approximations.

One of the simplest approximations is a model with finite number of chemically pre-identified phases. Let there be S known possible phases in the model. Each phase has a defined chemical composition $\mathbf{X}^j$, and a known Gibbs energy function $\bar{G}^j(P, T)$. The total composition of the system is $\mathbf{X}^0$ and we aim to constrain the

concentrations of the individual phases $\bar{\psi}^j$. Again it must hold, that

$$1 = \sum_{j=1}^{S} \bar{\psi}^j, \tag{2.8}$$

$$\mathbf{X}^0 = \sum_{j=1}^{S} \bar{\psi}^j \mathbf{X}^j. \tag{2.9}$$

The concentrations $\bar{\psi}^j$ complying with these conditions, must minimize the expression

$$\bar{g}_{P,T}(\{\bar{\psi}^j\}_{j=1}^S) = \sum_{j=1}^{S} \bar{\psi}^j \bar{G}^j(P,T), \tag{2.10}$$

in order for the system to be thermodynamically stable for given (P,T).

This expression is linear with respect to the vector of concentrations $\{\bar{\psi}^j\}_{j=1}^S$ and so are the restrictions (2.8,2.9) thus one can apply linear programming to find the solution. One particular example for a two-component system is shown in the Figure 2.2.

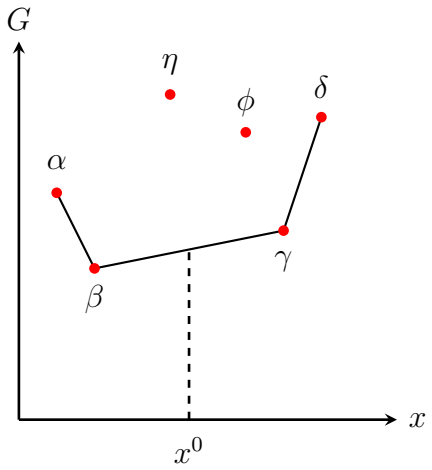

Figure 2.2: Example of 6 isochemical phases $\alpha, \beta, \gamma, \delta, \eta$, and ϕ in the $(G, \mathbf{X})$ space for a two-component mixture $\mathbf{X} = (x, 1-x)$. The black line represents the convex hull for given (P,T) conditions. For this particular choice of total composition $\mathbf{X}^0 = (x^0, 1-x^0)$, the system consists of a superposition of β and γ phases in accordance with the Gibbs phase rule.

Not all known phases have a fixed composition. This fact can be solved by the so called solution models. The basic idea to parametrize the solution as a superposition of a known set of p isochemical phases (end-points). The composition of a solution can be described by the barycentric coordinates in a p-simplex with the isochemical phases positioned in its vertices. The final Gibbs energy of the whole solution is then the weighted sum of the end-point values in the p-simplex corrected for the entropy of mixing term.

For computational purposes this parametrization is further discretized in a Cartesian manner into isochemical phases, which Connolly (2005) calls the pseudo-compounds. Then it is possible to increase the number of isochemical

phases considered in the system. The linear minimization then explores a more densely occupied $(G, \mathbf{X})$ space. An example of such parametrization in a two-component system is shown in the Figure 2.3. A detailed list of the solution phases considered in the Earth's mantle is discussed in the following section.

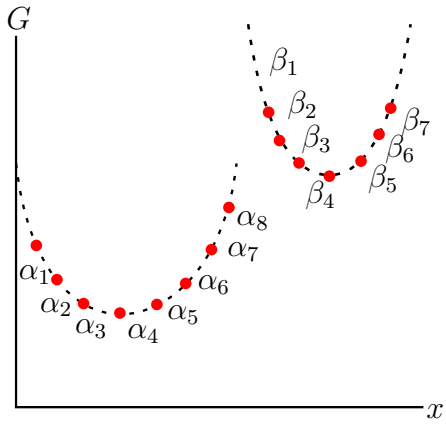

Figure 2.3: Solution models α and β represented in a two-component system. The solutions are respectively discretized into pseudo-compounds α_i and β_j. The values of G for $\alpha_2, \ldots, \alpha_7$ are interpolated from the end-point values α_1 and α_8 corresponding to the isochemical phases. Similar interpolation is applied also for β.

The Gibbs energy minimization is realized by the Perple_X software. Provided with a thermodynamic database describing the isochemical phases and database of the solution models, the Perple_X programs `verami` and `meemum` carry out the Gibbs energy minimization process for a given composition and (P, T) conditions. The resulting set of present phases and their concentrations is accompanied by selected physical properties, such as the seismic wave velocities and densities. However, the electrical conductivity of individual phases and the bulk electrical conductivity are not provided directly by Perple_X. Their calculation is the topic of Chapter 3 of this thesis. Further reading on the internal workings of `verami` and `meemum` programs can be found in Connolly (2009).

2.2 Mantle composition modelling

The chemical composition of the Earth's mantle can be, to some extent, described in the CFMASN model. It is a 6-dimensional space spanning all of the major mantle oxides: **C**aO, **F**eO, **M**gO, **A**l_2O_3, **S**iO_2, and **N**a_2O (Xu et al., 2008). Following a normalization, the composition can be parametrized just by a 5-dimensional vector. The dimensionality of the composition is further reduced to one by introduction of the basalt fraction f (Xu et al., 2008). The total composition vector is assembled as a linear combination of two fixed chemistries,

$$\mathbf{X}^0(f) = f\mathbf{X}^{\mathrm{B}} + (1-f)\mathbf{X}^{\mathrm{H}}.$$

Here $\mathbf{X}^{\mathrm{B}}$ and $\mathbf{X}^{\mathrm{H}}$ are the compositions of basalt and harzburgite in the CFMASN model, respectively. These two compositions are defined in the table 2.1.

Component	**Basalt**	**Harzburgite**
CaO	13,88	0,81
FeO	7,06	6,07
MgO	14,94	56,51
Al_2O_3	10,19	0,53
SiO_2	51,75	36,07
Na_2O	2,18	0,00

Table 2.1: Composition vectors of basalt and harzburgite in mol% after Xu et al. (2008).

One of the thermodynamic databases describing the Gibbs energies of the major mantle phases within the CFMASN model is constructed in Stixrude and Lithgow-Bertelloni (2005a,b). This database is available in Perple_X and is compatible with the default solution model file. Every Perple_X run needs a specific list of excluded isochemical phases and a list of permitted solution models. Following Khan (2016) I use the solution models summarized in the Table 2.2.

Solution phase	Chemical compositon	
ol[a]	$[Mg_xFe_{1-x}\ ]_2SiO_4$	$0 \leq x \leq 1$
wad[a]	$[Mg_xFe_{1-x}\ ]_2SiO_4$	$0 \leq x \leq 1$
ring[a]	$[Mg_xFe_{1-x}\ ]_2SiO_4$	$0 \leq x \leq 1$
C2/c px[a]	$[Mg_xFe_{1-x}\ ]_4Si_4O_{12}$	$0 \leq x \leq 1$
opx[a]	$[Ca_yFe_xMg_{1-x-y}\ ]_2$	
	$\cdot[Fe_xAl_yMg_{1-x-y}\ ]_2\ Si_4\ O_{12}$	$0 \leq x+y \leq 1$
cpx[a]	$[Ca_{1-x-y}Na_xMg_y\ ]_2$	
	$\cdot[Fe_wMg_{y+z}Al_{1-x-y-w-z}\ ]_2\ Si_4\ O_{12}$	$0 \leq x+y+z+w \leq 1$
gt[a]	$[\ (\ Na_{1/3}Al_{2/3}\ )_w\ Fe_xCa_yMg_{1-w-x-y}\ ]_3$	
	$\cdot[Mg_zAl_{1-z-w}Si_{w+z}\ ]_2\ Si_2\ O_{12}$	$0 \leq x+y+z+w \leq 1$
pv[b]	$Mg_xFe_{1-x-y}Al_{2y}Si_{1-y}O_3$	$0 \leq x+y \leq 1$
aki[a]	$Mg_xFe_{1-x-y}Al_{2y}Si_{1-y}O_3$	$0 \leq x+y \leq 1$
cf[a]	$Na_xMg_yFe_{1-x-y}Al_{2-x}Si_xO_4$	$0 \leq x+y \leq 1$
fp[a]	$Mg_xFe_{1-x}O$	$0 \leq x \leq 1$
stv	SiO_2	
ca-pv	$CaSiO_3$	

Table 2.2: Chemical composition of solutions and isochemical phases as in a)Xu et al. (2008) and b)Stixrude and Lithgow-Bertelloni (2007). The solution phase shortcuts are defined in the Chapter 3. Here w, x, y, z are the degrees of freedom.

The presence of water is not admitted within the framework of the CFMASN model. However, it plays an important role for the electrical conductivity of individual phases. After Khan (2016) I introduce the water content C_w as a separate parameter outside of the Gibbs energy minimization process. It is defined as a point-wise weight percentage of water present in the phase mix. The water is not evenly distributed in all of the resulting phases. The water partitioning is described in Khan (2016), but it is omitted here for the sake of simplicity.

3. Mantle rock conductivity

3.1 Charge transport mechanisms

Most of the present mantle phases are silica-based and can be considered semiconductors. Their conductivity spans the range of 6 orders of magnitude, from 10^{-7} S/m to 10^{-1} S/m (Simpson and Bahr, 2005, Figure 1.5).

There are three charge transport mechanisms contributing to the total conductivity of mantle phases: the ionic conductivity σ_i, the proton conductivity σ_p, and the small polaron hopping conductivity σ_h (Yoshino, 2010). All of these mechanisms, if present, act in a parallel manner and the total conductivity of the phase is

$$\sigma = \sigma_i + \sigma_p + \sigma_h \,. \tag{3.1}$$

The ionic conductivity is the most simple conducting mechanism in mantle minerals. It is caused by the movement of ions between vacancies in the crystal lattice. A specific type of ionic conductivity is proton conductivity. It typically depends on the water content in the mineral. The water here provides the positive hydrogen ion as a charge transporting particle, where the proton hops between point defects in the crystal lattice.

In the case of small polaron hopping the charge carrier is a quasi particle called polaron, that moves (hops) between iron sites in the phase solution. Thus the strength of the mechanism depends on the amount of iron in the mineral. The theory of small polaron hopping is further described in Triberis (2017). The iron content X_{Fe} is defined as a dimensionless coefficient referenced as the lower index of Fe as in the Table 2.2.

Each conductivity term in the equation (3.1) depends also on temperature, and pressure. These dependencies can be parametrized by the activation energy (or enthalpy) and the activation volume in an Arrhenius-like expression. Their values as well as their dependencies on the water and iron content are determined experimentally from high pressure and temperature conductivity measurements. Note, that following Khan (2016) I ommit the effect of oxygen fugacity on the phase conductivity.

3.2 Experimental conductivities

3.2.1 Olivine

The olivine (ol) conductivity is the best example to demonstrate the experimental relations at play. The temperature dependence for the ionic conductivity,

$$\sigma_i = \exp\left(\ln(10)\log_{10}\left(\sigma_{0i}\right) - \frac{H_i}{k_B T}\right), \tag{3.2}$$

is obtained from Yoshino et al. (2009). The awkward use of $\log_{10}\left(\sigma_{0i}\right)$ emphasizes, that the base conductivity σ_{0i} and it's error estimate are provided on the logarithmic scale. Here H_i represents the activation enthalpy and k_B is the Boltzmann constant.

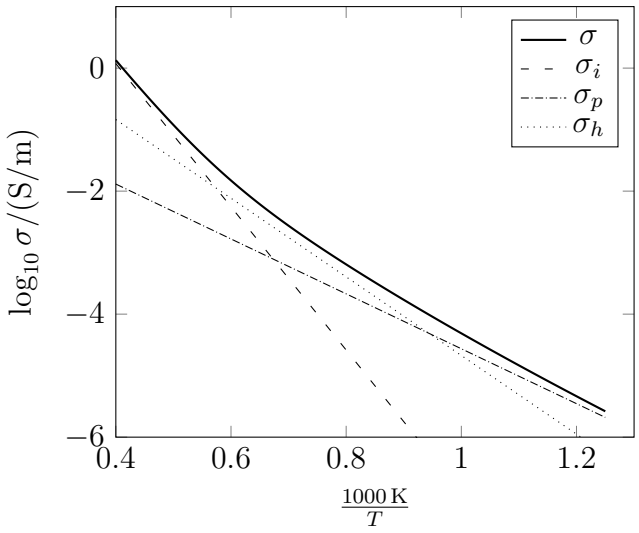

Figure 3.1: Experimental conductivity relations for wet ($C_w = 0.01\%$) iron bearing ($X_{\mathrm{Fe}} = 0.1$) olivine. The total conductivity σ is decomposed into the ion conductivity σ_i, the proton conductivity σ_p, and the small polaron conductivity σ_h.

Yoshino et al. (2009) also provides the proton conductivity relation,

$$\sigma_p = C_w \exp\left(\ln(10)\log_{10}(\sigma_{0p}) - \frac{H_{0p} - \alpha_p C_w^{1/3}}{k_B T}\right), \tag{3.3}$$

where the coefficient α_p controls the modification of the base enthalpy H_{0p} by the water content C_w. Here σ_{0p} denotes the base proton conductivity.

The small polaron conductivity parametrization,

$$\sigma_h = X_{\mathrm{Fe}}\sigma_{0h} \exp\left(-\frac{E_{0h} - \alpha_h X_{\mathrm{Fe}}^{1/3} + P(V_{0h} - \beta_h X_{\mathrm{Fe}})}{k_B T}\right), \tag{3.4}$$

is governed by the base activation energy E_{0h}, base activation volume V_{0h} and their respective iron content modifiers α_h, and β_h (Yoshino et al., 2012). Note that the small polaron hopping base conductivity σ_{0h} is provided on a linear scale with it's error estimate.

The numerical values of individual parameters for olivine are presented in tables 3.1, 3.2, and 3.3. Figure 3.1 illustrates the temperature dependencies of the experimental relations for wet iron bearing olivine. Each charge transport mechanism dominates in a given temperature range due to different activation enthalpies, energies and volumes.

	$\log_{10}(\sigma_{0i}\,[\mathrm{S/m}])$	$H_i\,[\mathrm{eV}]$
ol	4.73 ± 0.53	2.31 ± 0.07

Table 3.1: Base ion conductivity and activation energy for olivine after Yoshino et al. (2009).

	$\log_{10}(\sigma_{0p}\,[\mathrm{S/m}])$	$H_{0p}\,[\mathrm{eV}]$	$\alpha_p\,[\mathrm{eV}]$
ol	1.90 ± 0.44	0.92 ± 0.04	0.16 ± 0.02
opx	2.58 ± 0.14	0.84 ± 0.03	0.08 ± 0.03

Table 3.2: Base proton conductivity and activation enthalpy coefficients for olivine and orthopyroxene after Yoshino et al. (2009) and Zhang et al. (2012), respectively.

	$\sigma_{0h}\,[\mathrm{S/m}]$	$E_{0h}\,[\mathrm{eV}]$	$\alpha_h\,[\mathrm{eV}]$	$V_{0h}\,[\mathrm{cm^3/mol}]$	$\beta_h\,[\mathrm{cm^3/mol}]$
ol	525 ± 37	1.96 ± 0.02	1.49 ± 0.03	-0.01 ± 0.04	0.22 ± 0.34
ring	1885 ± 572	1.96 ± 0.14	1.46 ± 0.16	-0.33 ± 0.44	0.72 ± 0.55
fp	19.0 ± 1.0	0.63 ± 0.01	0.66 ± 0.03	-0.45 ± 0.01	0.61 ± 0.14

Table 3.3: Base small polaron hopping conductivity, activation energy and activation volume coefficients for olivine and ringwoodite after Yoshino et al. (2012) and ferropericlase after Yoshino et al. (2011).

3.2.2 Wadsleyite

The water dependent proton conductivity relation of wadsleyite (wad),

$$\sigma_p = C_w \sigma_{0p} \exp\left(-\frac{H_{0p} - \alpha_p C_w^{1/3}}{k_B T}\right), \tag{3.5}$$

is almost identical to the equation (3.3). The only difference is the presence of σ_{0p} on a linear scale (Yoshino and Katsura, 2012a,b).

The small polaron hopping conductivity relation presented in Yoshino and Katsura (2012a),

$$\sigma_h = \sigma_{0h} \exp\left(-\frac{H_h}{k_B T}\right), \tag{3.6}$$

doesn't depend on iron content. Yoshino and Katsura (2012a) states, that small polaron hopping conductivity is sensitive to iron content. However, the iron content range for wadsleydite is too narrow for exploring this dependency.

Numerical values of conductivity parameters for wadslyite are presented in Tables 3.4 and 3.5 after an erratum by Yoshino and Katsura (2012b) to the original article (Yoshino and Katsura, 2012a).

	$\sigma_{0p}\,[\mathrm{S/m}]$	$H_{0p}\,[\mathrm{eV}]$	$\alpha_p\,[\mathrm{eV}]$
wad	25 ± 3	0.83 ± 0.02	0.02 ± 0.02
ring	27.7 ± 9.6	1.12 ± 0.03	0.67 ± 0.03

Table 3.4: Base proton conductivity and activation energy coefficients for wadsleydite and ringwoodite after Yoshino and Katsura (2012b) and Yoshino et al. (2008a), respectively.

	σ_{0h} [S/m]	H_h [eV]
wad	288 ± 38	1.45 ± 0.02

Table 3.5: Base small polaron hopping conductivity and activation enthalpy for wadsleydite after Yoshino and Katsura (2012b).

3.2.3 Ringwoodite

Ringwoodite (ring) exhibits the water dependent proton conductivity presented in Yoshino et al. (2008a) described by the equation (3.5). The small polaron hopping conductivity for ringwoodite was obtained from Yoshino et al. (2012) in the form of the equation (3.4). Numerical values of coefficients governing both of these mechanisms are presented in Tables 3.3 and 3.4.

3.2.4 Clinopyroxene and its C2/c polymorph

The total electrical conductivity of clinopyroxene (cpx) is summarized by Arrhenius equation

$$\sigma = \exp\left(\ln(10)\log_{10}(\sigma_0) - \frac{H}{k_B T}\right), \tag{3.7}$$

where the base conductivity σ_0 and activation enthalpy H are summarized in the Table 3.6 (Xu and Shankland, 1999). Note, that no particular charge transport mechanism is specified in Xu and Shankland (1999). According to Khan et al. (2006) the same relation can be used for the C2/c clinopyroxen polymorph.

	$\log_{10}(\sigma_0\,[\mathrm{S/m}])$	H [eV]
cpx	3.25 ± 0.11	1.87 ± 0.02
pv	1.87 ± 0.11	0.70 ± 0.04

Table 3.6: The base conductivity and the activation energy for clinopyroxene and perovskite after Xu and Shankland (1999) and Yousheng et al. (1998), respectively.

3.2.5 Orthopyroxene

According to Zhang et al. (2012), the electrical conductivity of otrhopyroxene (opx), is composed of the proton conductivity and the iron content independent small polaron hopping conductivity described by equations (3.3) and (3.8), respectively. The corresponding coefficients are presented in the Tables 3.2 and 3.7.

$$\sigma = \exp\left(\ln(10)\log_{10}(\sigma_{0h}) - \frac{H_h}{k_B T}\right) \tag{3.8}$$

	$\log_{10}(\sigma_{0h}\,[\mathrm{S/m}])$	$H_h\,[\mathrm{eV}]$
opx	3.25 ± 0.11	1.87 ± 0.02

Table 3.7: The base conductivity and the activation energy for orthopyroxene after Zhang et al. (2012).

3.2.6 Garnet

A simplified experimental temperature dependent Arrhenius conductivity relation for garnet (gt), covering all relevant charge transport mechanisms, is provided by Yoshino et al. (2008b). The conductivity has the form

$$\sigma_h = \sigma_0(T) \exp\left(-\frac{E(T)}{k_B T}\right). \tag{3.9}$$

However, the base conductivity and the activation energy are temperature dependent functions approximated by piecewise constant or linear expressions,

$$\sigma_0(T) = \begin{cases} \sigma_{01} & 900 < T < 1300, \\ \sigma_{02} & 1300 < T < 1750, \\ \frac{(1800-T)\sigma_{02}+(T-1750)\sigma_{03}}{50} & 1750 < T < 1800, \\ \sigma_{03} & 1800 < T < 2000, \end{cases} \tag{3.10}$$

$$E(T) = \begin{cases} E_{01} & 900 < T < 1300, \\ E_{02} & 1300 < T < 1750, \\ \frac{(1800-T)E_{02}+(T-1750)E_{03}}{50} & 1750 < T < 1800, \\ E_{03} & 1800 < T < 2000. \end{cases} \tag{3.11}$$

The numerical values of the coefficients used here are presented in the Table 3.8. The measurements for the conductivity parameters in Yoshino et al. (2008b) are provided for the three distinct temperature intervals. I take the liberty to linearly interpolate the coefficients in the temperature gap.

	$\sigma_{01}\,[\mathrm{S/m}]$	$\sigma_{02}\,[\mathrm{S/m}]$	$\sigma_{03}\,[\mathrm{S/m}]$	$E_{01}\,[\mathrm{eV}]$	$E_{02}\,[\mathrm{eV}]$	$E_{03}\,[\mathrm{eV}]$
gt	54	1070	17560	1.27	1.59	2.02

Table 3.8: The conductivity coefficients and the activations for garnet after Yoshino et al. (2008b).

3.2.7 Perovskite and Calcium-perovskite

I use simple Arrhenius conductivity for perovskite (pv) and calcium-perovskite (ca-pv) from Yousheng et al. (1998) in the form of the equation (3.7) with coefficients in Table 3.6. The same conductivity model was used for the solution model perovskite and the its isochemical endpoint calcium-perovskite.

3.2.8 Akimotoite

For akimotoite (aki) I use the pressure dependent conductivity relation

$$\sigma = \sigma_0 \exp\left(-\frac{E + VP}{k_B T}\right), \tag{3.12}$$

obtained from Katsura et al. (2007) with coefficients in the Table 3.9.

	σ_0	E [eV]	V [cm^3/mol]
aki	15 ± 5	0.82 ± 0.06	-1.5 ± 0.02

Table 3.9: Base conductivity and activation energy for akimotoite after Katsura et al. (2007).

3.2.9 Calcium ferrite

As in Khan et al. (2011) I omit the contribution of calcium ferrite (ca-f) to the bulk conductivity, thus excluding it in the later described averaging algorithm.

3.2.10 Ferropericlase

Small polaron hopping conductivity in the form of the equation 3.4 is used for ferropericlase (fp) with coefficients in the Table 3.3 obtained from Yoshino et al. (2011).

3.2.11 Stishovite

For stishovite (stv), following Yoshino et al. (2014), I employ the water dependent proton conductivity in the form of equation (3.5) with coefficients in the Table 3.4.

3.3 Bulk conductivity

Knowing the conductivities of present phases is just the first piece of the puzzle. The second one is to combine the phase conductivities into the total bulk conductivity of the phase mixture. The bulk conductivity depends on the conductivities and volume fractions of the individual phases. For phases $j = 1, \ldots, s$ I denote the phase conductivities $\sigma_1, \ldots, \sigma_s$ and their volume fractions $c_1, \ldots, c_s$, which are related to the phase concentrations $\bar{\psi}^j$ through the scaling

$$c_j = \frac{M^j \bar{\psi}^j}{\rho^j} \Big/ \left(\sum_{i=1}^{s} \frac{M^i \bar{\psi}^i}{\rho^i}\right). \tag{3.13}$$

Here M^j is the molar weight and ρ^j is the density of the j-th phase. The volume fractions are provided directly by Perple_X. If a phase is omitted from the calculation, like in the case of calcium ferrite, I set its volume fraction to zero and renormalize the rest.

The bulk conductivity can be obtained in infinitely many ways, depending on the spatial structure of the phase mixture and the direction of the electric current. Assuming isotropic and entropic configuration of the phases, the upper and the lower bounds of the bulk conductivity, so-called Hashin-Shtrikman (HS) bounds, can be calculated. The solution for multiphase electric conductivity HS bounds is derived from Hashin and Shtrikman (1962), following Khan (2016),

$$\sigma_{\mathrm{HS}\pm} = \left[\sum_{j=1}^{s} \frac{c_j}{\sigma_j + 2\sigma_\pm}\right]^{-1} - 2\sigma_\pm. \tag{3.14}$$

Here $\sigma_{\mathrm{HS}\pm}$ denote the conductivity values for the lower HS_- and upper HS_+ bounds. The minimum and maximum conductivities present in the phase mixture are denoted by σ_- and σ_+, respectively.

The sought bulk conductivity averaging algorithm should consistently provide values between the HS bounds. One such average is the self-consistent (SC) average used in Khan (2016). It is defined by an implicit formula

$$\sum_{j=1}^{s} c_j \left[\frac{\sigma_j - \sigma_{\mathrm{SC}}}{\sigma_j + 2\sigma_{\mathrm{SC}}}\right] = 0. \tag{3.15}$$

The value for the SC average can be obtained by finding the only real positive root of a polynomial equation. This process can be done numerically.

Figure 3.2 illustrates the properties of the HS bounds and the SC average for a simplified example of a two-phase mixture. Note that the weighted arithmetic average σ_{P}, also shown in the figure, lies outside the range of the HS bounds.

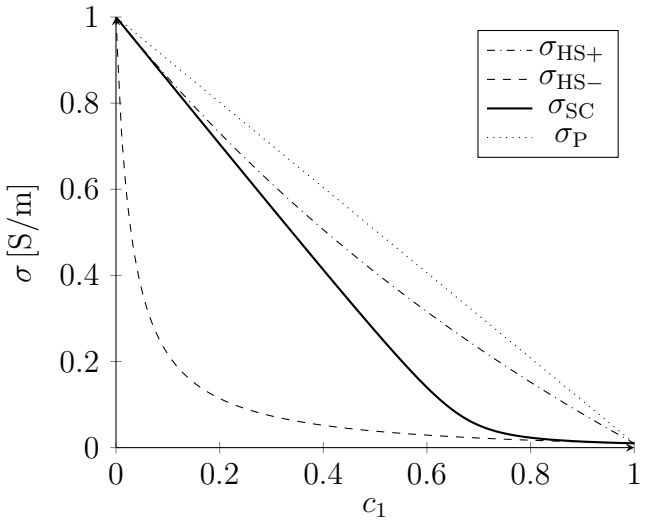

Figure 3.2: The HS bounds $\sigma_{\mathrm{HS}\pm}$, the SC average σ_{SC}, and the weighted arithmetic average σ_{P} for a two phase mixture. The phases have the electrical conductivities $\sigma_1 = 0.01\,\mathrm{S/m}$ and $\sigma_2 = 1\,\mathrm{S/m}$ and volume fractions c_1 and $c_2 = 1 - c_1$, respectively.

3.4 Point-wise implementation

The basic structure of the code is represented by the scheme in the Figure 3.3. The main program passes the values of the temperature T, the pressure P, the

chemical composition $\mathbf{X}$ (represented by the basalt fraction f) and the water content C_w to the point-wise forward problem routine. The routine uses the Perple_X subroutine `meemum` to obtain the list of present phases p and their respective volume fractions $\vec{c}$ in the mixture. The module `sigma_model`, which I wrote in Fortran 90, implements all of the conductivity relations for individual phases as described in the Chapter 3. The modular structure allows for easy updates of the experimental-based parameters and future additions (e.g, the post-perovskite phase (Ohta et al., 2008, 2010)). For each present phase, the electrical conductivity is thus retrieved at given (P, T, C_w) conditions and taking into account the concentrations of iron X_{Fe} in the individual pseudo-compounds. The implementation of the conductivity modules for all individual phases has been thoroughly tested against the models of Khan (2016) and compared to respective experimental references. Using these values and the volume fractions $\vec{c}$ the Fortran 90 module `sigma_bulk` calculates the bulk conductivity in the sense of the SC average.

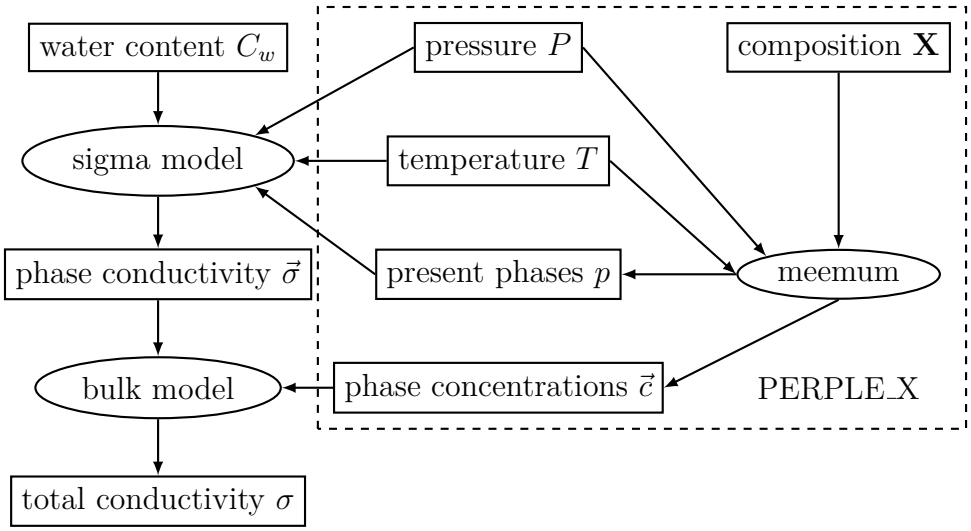

Figure 3.3: Diagram showing a single point-wise computation of the bulk conductivity σ for given T, P, $\mathbf{X}$ and C_w.

Note that the iron content X_{Fe} is not explicitly included within the Figure 3.3. However it is implicitly contained within the definition of the resulting phases p. Additional Perple_X subroutines, `input1`, `input2`, `setau1`, `input9` and `initlp`, are used for the initialization of the thermodynamical and solution-model data files.

4. Results

Whereas the Chapters 2 and 3 describe the point-wise calculation of electrical conductivity for given (P, T, f, C_w) conditions, the purpose of this chapter is to put these results in the context of the spherically symmetric Earth's mantle. First I demonstrate the ability of the method to predict a realistic 1-D mantle conductivity profile for geophysically relevant inputs. The prescribed dependence of pressure P on the depth h is derived from the density distribution of the **PR**eliminary **E**arth **M**odel (Dziewonski and Anderson, 1981). I set a constant water content $C_w = 0.01\%$, and following Khan (2016) I set the basalt content $f = 0.2$ above 410 km and $f = 0.8$ below. The geotherm $T(h)$, presented in the Figure 4.1b, is adapted from Brown and Shankland (1981) with surface temperature set to 0 °C. In the Figure 4.1a, the predicted conductivity Model A is shown with a solid black line.

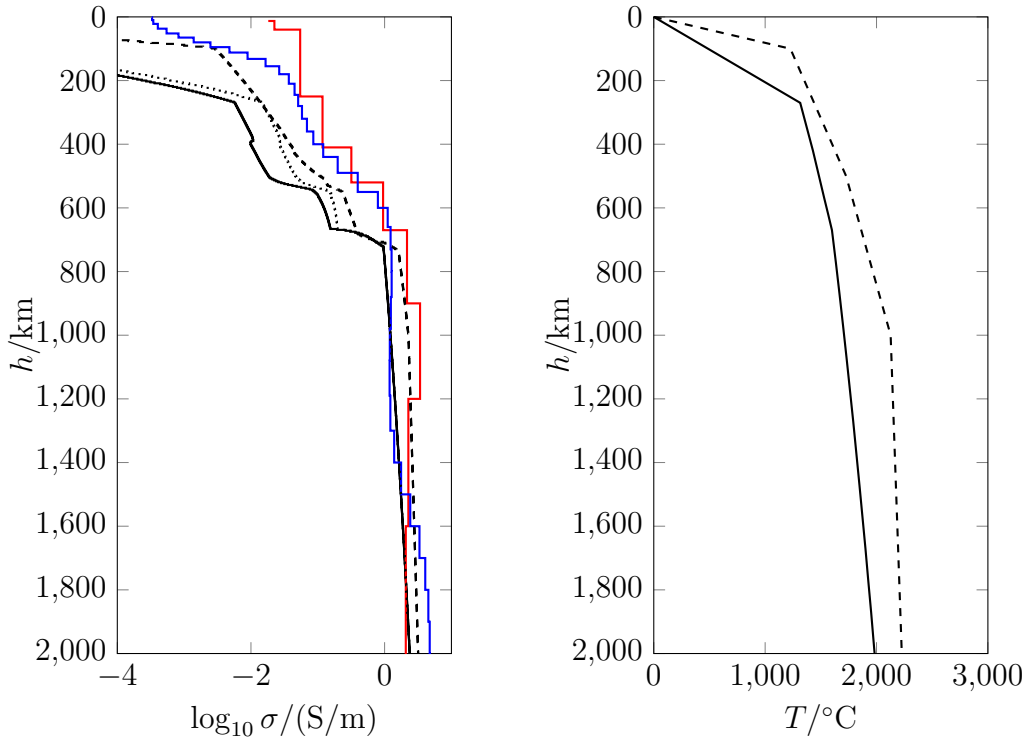

(a) The 1-D conductivity profiles. The CUP20-0S6 (solid red line) and MIN1D_0501 (solid blue line) are observation-based models. Model A (solid black line) is the result of the thermochemical forward modelling using the Brown and Shankland (1981) geotherm. Model B (dashed black line) is based on the adjusted geotherm. Model C (dotted black line) uses the original geotherm, but changes water content to $C_w = 1\%$

(b) Temperature-depth dependence for the Brown and Shankland (1981) geotherm (solid line) and the ad-hoc adjusted geotherm (dashed line).

Figure 4.1: The depth-conductivity and the depth-temperature dependencies.

Two electrical conductivity models obtained by inversion of electromagnetic data are also shown in the Figure 4.1a for comparison. The MIN1DM_0501 model (solid blue line) was obtained by joint inversion of two datasets in the frequency domain. First, the C-responses (Simpson and Bahr, 2005), which are the electromagnetic transfer functions describing the Earth's mantle reaction to the ring current variations in the magnetosphere, were obtained by analysis of Swarm satellite geomagnetic data. Second, the satellite observations of signals induced by tidally-forced ocean currents were also included in the inversion to improve the model resolution from the lithosphere down to the mantle transition zone. Detailed description of the method is provided by Grayver et al. (2017), the actual model is a result of processing of 5 years of Swarm observations[1]. The next conductivity model, denoted as CUP20-OS6 in Figure 4.1a (solid red line) is based on the time-domain inversion of 6 years of Swarm data, supported by surface observatories. Although the CUP20-OS6 is a 3-D model, which includes also the lateral variations of electrical conductivity, here I use only the spherically symmetric component of the model. The details of the model are described by Velímský and Knopp (2021).

An overview of constructed modeles is presented in the Table 4.1 with their respective values of water content and geotherms. From the Figure 4.1a it is obvious, that the Model A is significantly more resistive than the observation-based models in the upper mantle. However, there is good agreement between the respective models in the lower mantle.

The full inversion of the observation-based conductivities in terms of the thermochemical and mineralogical state of the mantle is beyond the scope of this thesis. To illustrate the sensitivity of the forward problem to the geotherm I present the Model B, shown in the Figure 4.1a with a black dashed line. This model is obtained for an ad-hoc adjusted geotherm, shown by a dashed line in the Figure 4.1b. The $P(h)$, C_w and f parameters remain unchanged. The steeper geothermal gradient in the upper mantle yields a better agreement with the observation-based models. On the other hand, the Model C, shown by the dotted black line in the Figure 4.1a, is obtained for the original geotherm of Brown and Shankland (1981) with the water content increased to $C_w = 1\%$. The effect of water content on the conductivity profile is notable in the transition zone.

Model	C_w	Goetherm
A	0.01%	BS81
B	0.01%	ad hoc
C	1%	BS81

Table 4.1: A list of the forward models with their respective values of water content and geotherms. The geotherm in Brown and Shankland (1981) is abbreviated as BS81.

[1] `https://swarm-diss.eo.esa.int/#swarm%2FLevel2longterm%2FMIN`

Conclusions and outlook

I have developed two Fortran 90 modules, `sigma_model` and `sigma_bulk`, coupled to the Perple_X software. I have demonstrated how this method can create a 1-D conductivity model comparable to those obtained from the inversion of EM data. The point-wise structure of the code allows for future implementations to 1-D and 3-D inversion of EM data and interpretation of conductivity models.

One run of the point-wise computation on a single thread on the current generation of PCs takes approximately a few milliseconds and there is a room for future multi-thread parallelization. This relatively fast runtime does not create a computational bottleneck for future use in an EM inversion scheme, like the one in Velímský and Knopp (2021), which takes up to several orders of magnitude more computer time. This speed also allows for a Bayesian methods of parameter space exploration e.g., simulated annealing, parallel tempering, or other modern algorithms based on the Metropolis-Hastings rule (Sambridge, 2014). The runtime could be further decreased by precalculating the bulk conductivity in the (P, T, C_w, f) space.

The modular structure allows for easy correction of the database for new experimental high-pressure conductivity measurements. Furthermore it is possible to expand the conductivity database for other phases, like the high-pressure post-perovskite, present in the D'' layer (Ohta et al., 2008, 2010). This can be used for constraining the conductivity in the lowermost parts of the Earth's mantle. One of the challenges for this method is to encompass the high-conductivity partial melts present in the upper mantle (Khan, 2016; Martinec et al., 2021).

There are several ways how to use this method in an EM inversion scheme. The first is to construct an a priori estimate of the conductivity model, like in Martinec et al. (2021), and use it as a regularization for the inversion scheme. The second is to invert the electrical conductivity constrained by EM data in the sense of temperature and compositional structure of the mantle, and it is also possible to directly invert the EM data in terms of a thermal and compositional model, like the one in Khan (2016).

The last two applications are challenged by overparametrization, meaning that the single result of the forward problem depends on multiple thermochemical parameters. This ambiguity can cause significant problems in the global inversion scheme, if the parameters are not regularized. Luckily the electrical conductivity is not the only output of the thermochemical modelling. Whereas I use only the phase information and the volume fractions, the Perple_X also provides most of the aforementioned material properties, like P and S seismic wave velocities and densities. This additional data can be used in a global coupled inversion of electromagnetic, gravitational, thermal and seismic data.

In the near future there will be growing interest in performing this type of joint inversions, as more geophysical dataset become available. For EM studies, we expect additional data from non-dedicated platform magnetometers, like that on CryoSat-2 used in Velímský and Knopp (2021), annual data updates from the current Swarm mission satellites, and finally the data from the NanoMagSat, with tentative launch date in 2023 (Hulot et al., 2018).

Bibliography

Brown, J. M. and Shankland, T. J. Thermodynamic parameters in the earth as determined from seismic profiles. *Geophysical Journal of the Royal Astronomical Society*, 66(3):579–596, 1981. doi: https://doi.org/10.1111/j.1365-246X.1981.tb04891.x. URL https://onlinelibrary.wiley.com/doi/abs/10.1111/j.1365-246X.1981.tb04891.x.

Connolly, J. Multivariable phase diagrams: an algorithm based on generalized thermodynamics. *American Journal of Science*, 290(6):666–718, 1990. ISSN 00029599. URL https://search.ebscohost.com/login.aspx?authtype=shib&custid=s1240919&profile=eds.

Connolly, J. Computation of phase equilibria by linear programming: A tool for geodynamic modeling and its application to subduction zone decarbonation. *Earth and Planetary Science Letters*, 236(1):524–541, 2005. ISSN 0012-821X. doi: https://doi.org/10.1016/j.epsl.2005.04.033. URL https://www.sciencedirect.com/science/article/pii/S0012821X05002839.

Connolly, J. The geodynamic equation of state: What and how. *Geochemistry, Geophysics, Geosystems*, 10(10), 2009. doi: https://doi.org/10.1029/2009GC002540. URL https://agupubs.onlinelibrary.wiley.com/doi/abs/10.1029/2009GC002540.

Dziewonski, A. and Anderson, D. Preliminary reference earth model. *Phys. Earth Plan. Int.*, pages 297–356, 1981. doi: 10.17611/DP/9991844.

Fullea, J., Lebedev, S., Martinec, Z., and Celli, N. L. WINTERC-G: mapping the upper mantle thermochemical heterogeneity from coupled geophysical–petrological inversion of seismic waveforms, heat flow, surface elevation and gravity satellite data. *Geophysical Journal International*, 226(1):146–191, 03 2021. ISSN 0956-540X. doi: 10.1093/gji/ggab094. URL https://doi.org/10.1093/gji/ggab094.

Grayver, A. V., Munch, F. D., Kuvshinov, A. V., Khan, A., Sabaka, T. J., and Tøffner-Clausen, L. Joint inversion of satellite-detected tidal and magnetospheric signals constrains electrical conductivity and water content of the upper mantle and transition zone. 44:6074–6081, 2017.

Hashin, Z. and Shtrikman, S. A variational approach to the theory of the effective magnetic permeability of multiphase materials. *Journal of Applied Physics*, 33 (10):3125–3131, 1962. doi: 10.1063/1.1728579. URL https://doi.org/10.1063/1.1728579.

Hulot, G., Leger, J. M., Vigneron, P., Jager, T., Bertrand, F., Coïsson, P., Deram, P., Boness, A., Laurens, A., and Faure, B. The NanoMagSat Nanosatellite High-Precision Magnetic Project. In *AGU Fall Meeting Abstracts*, volume 2018, pages A41K–3116, Dec. 2018.

Katsura, T., Yokoshi, S., Kawabe, K., Shatskiy, A., Okube, M., Fukui, H., Ito, E., Nozawa, A., and Funakoshi, K.-i. Pressure dependence of electrical conductivity of (mg,fe)sio3 ilmenite. *Physics and Chemistry of Minerals*, 34(4): 249–255, May 2007. ISSN 1432-2021. doi: 10.1007/s00269-007-0143-0. URL https://doi.org/10.1007/s00269-007-0143-0.

Khan, A. On earth's mantle constitution and structure from joint analysis of geophysical and laboratory-based data: An example. *Surveys in Geophysics*, 37(1):149–189, Jan 2016. ISSN 1573-0956. doi: 10.1007/s10712-015-9353-z. URL https://doi.org/10.1007/s10712-015-9353-z.

Khan, A., Connolly, J., and Olsen, N. Constraining the composition and thermal state of the mantle beneath europe from inversion of long-period electromagnetic sounding data. *Journal of Geophysical Research: Solid Earth*, 111(B10), 2006. doi: https://doi.org/10.1029/2006JB004270. URL https://agupubs.onlinelibrary.wiley.com/doi/abs/10.1029/2006JB004270.

Khan, A., Kuvshinov, A., and Semenov, A. On the heterogeneous electrical conductivity structure of the earth's mantle with implications for transition zone water content. *Journal of Geophysical Research: Solid Earth*, 116(B1), 2011. doi: https://doi.org/10.1029/2010JB007458. URL https://agupubs.onlinelibrary.wiley.com/doi/abs/10.1029/2010JB007458.

Kuvshinov, A. Global 3-D EM studies of the solid Earth: Progress status. In Spichak, V. V., editor, *Electromagnetic Sounding of the Earth's Interior*, pages 1 – 21. Elsevier, Boston, second edition, 2015.

Kuvshinov, A., Grayver, A., Tøffner-Clausen, L., and Olsen, N. Probing 3-d electrical conductivity of the mantle using 6 years of swarm, cryosat-2 and observatory magnetic data and exploiting matrix q-responses approach. *Earth, Planets and Space*, 73(1):67, Mar 2021. ISSN 1880-5981. doi: 10.1186/s40623-020-01341-9. URL https://doi.org/10.1186/s40623-020-01341-9.

Martinec, Z., Fullea, J., Velímský, J., and Šachl, L. A new integrated geophysical-petrological global 3-D model of upper-mantle electrical conductivity validated by the Swarm M2 tidal magnetic field. *Geophysical Journal International*, 226(2):742–763, 04 2021. ISSN 0956-540X. doi: 10.1093/gji/ggab130. URL https://doi.org/10.1093/gji/ggab130.

Ohta, K., Onoda, S., Hirose, K., Sinmyo, R., Shimizu, K., Sata, N., Ohishi, Y., and Yasuhara, A. The electrical conductivity of post-perovskite in earth's d'' layer. *Science*, 320(5872):89–91, 2008. ISSN 0036-8075. doi: 10.1126/science.1155148. URL https://science.sciencemag.org/content/320/5872/89.

Ohta, K., Hirose, K., Ichiki, M., Shimizu, K., Sata, N., and Ohishi, Y. Electrical conductivities of pyrolitic mantle and morb materials up to the lowermost mantle conditions. *Earth and Planetary Science Letters*, 289(3):497–502, 2010. ISSN 0012-821X. doi: https://doi.org/10.1016/j.epsl.2009.11.042. URL https://www.sciencedirect.com/science/article/pii/S0012821X09007043.

Sambridge, M. A Parallel Tempering algorithm for probabilistic sampling and multimodal optimization. *Geophysical Journal International*, 196(1):357–374, 10 2014. ISSN 0956-540X. doi: 10.1093/gji/ggt342. URL https://doi.org/10.1093/gji/ggt342.

Simpson, F. and Bahr, K. *Practical Magnetotellurics*. Cambridge University Press, 2005. doi: 10.1017/CBO9780511614095.

Stixrude, L. and Lithgow-Bertelloni, C. Mineralogy and elasticity of the oceanic upper mantle: Origin of the low-velocity zone. *Journal of Geophysical Research: Solid Earth*, 110(B3), 2005a. doi: https://doi.org/10.1029/2004JB002965. URL https://agupubs.onlinelibrary.wiley.com/doi/abs/10.1029/2004JB002965.

Stixrude, L. and Lithgow-Bertelloni, C. Thermodynamics of mantle minerals — I. Physical properties. *Geophysical Journal International*, 162(2):610–632, 08 2005b. ISSN 0956-540X. doi: 10.1111/j.1365-246X.2005.02642.x. URL https://doi.org/10.1111/j.1365-246X.2005.02642.x.

Stixrude, L. and Lithgow-Bertelloni, C. Influence of phase transformations on lateral heterogeneity and dynamics in earth's mantle. *Earth and Planetary Science Letters*, 263(1):45–55, 2007. ISSN 0012-821X. doi: https://doi.org/10.1016/j.epsl.2007.08.027. URL https://www.sciencedirect.com/science/article/pii/S0012821X07005377.

Triberis, G. P. *Small Polaron Hopping DC Conductivity in 3D and 1D Disordered Materials.* Materials Science and Technologies. Nova Science Publishers, Inc, 2017. ISBN 9781536119435. URL https://search.ebscohost.com/login.aspx?authtype=shib&custid=s1240919&profile=eds.

Velímský, J. Determination of three-dimensional distribution of electrical conductivity in the Earth's mantle from Swarm satellite data: Time-domain approach. 65:1239–1246, 2013.

Velímský, J. and Knopp, O. Lateral variations of electrical conductivity in the lower mantle constrained by swarm and cryosat-2 missions. *Earth, Planets and Space*, 73(1):4, Jan 2021. ISSN 1880-5981. doi: 10.1186/s40623-020-01334-8. URL https://doi.org/10.1186/s40623-020-01334-8.

Velímský, J. and Martinec, Z. Time-domain, spherical harmonic-finite element approach to transient three-dimensional geomagnetic induction in a spherical heterogeneous Earth. 160:81–101, 2005.

Velímský, J., Grayver, A., Kuvshinov, A., and Šachl, L. On the modelling of M_2 tidal magnetic signatures: Effects of physical approximations and numerical resolution. *Earth, Planets and Space*, 70:192, 2018. doi: 10.1186/s40623-018-0967-5.

Xu, W., Lithgow-Bertelloni, C., Stixrude, L., and Ritsema, J. The effect of bulk composition and temperature on mantle seismic structure. *Earth and Planetary Science Letters*, 275(1):70–79, 2008. ISSN 0012-821X. doi: https://

doi.org/10.1016/j.epsl.2008.08.012. URL https://www.sciencedirect.com/science/article/pii/S0012821X08005281.

Xu, Y. and Shankland, T. J. Electrical conductivity of orthopyroxene and its high pressure phases. *Geophysical Research Letters*, 26(17):2645–2648, 1999. doi: https://doi.org/10.1029/1999GL008378. URL https://agupubs.onlinelibrary.wiley.com/doi/abs/10.1029/1999GL008378.

Yoshino, T. Laboratory electrical conductivity measurement of mantle minerals. *Surveys in Geophysics*, 31(2):163–206, Mar 2010. ISSN 1573-0956. doi: 10.1007/s10712-009-9084-0. URL https://doi.org/10.1007/s10712-009-9084-0.

Yoshino, T. and Katsura, T. Re-evaluation of electrical conductivity of anhydrous and hydrous wadsleyite. *Earth and Planetary Science Letters*, 337-338:56–67, 2012a. ISSN 0012-821X. doi: https://doi.org/10.1016/j.epsl.2012.05.023. URL https://www.sciencedirect.com/science/article/pii/S0012821X1200249X.

Yoshino, T. and Katsura, T. Erratum to: Re-evaluation of electrical conductivity of anhydrous and hydrous wadsleyite [earth planet. sci. lett. 337–338 (1) (2012) 56–67]. *Earth and Planetary Science Letters*, 357-358:422, 2012b. ISSN 0012-821X. doi: https://doi.org/10.1016/j.epsl.2012.10.020. URL https://www.sciencedirect.com/science/article/pii/S0012821X1200581X.

Yoshino, T., Manthilake, G., Matsuzaki, T., and Katsura, T. Dry mantle transition zone inferred from the conductivity of wadsleyite and ringwoodite. *Nature*, 451(7176):326–329, Jan 2008a. ISSN 1476-4687. doi: 10.1038/nature06427. URL https://doi.org/10.1038/nature06427.

Yoshino, T., Nishi, M., Matsuzaki, T., Yamazaki, D., and Katsura, T. Electrical conductivity of majorite garnet and its implications for electrical structure in the mantle transition zone. *Physics of the Earth and Planetary Interiors*, 170(3):193–200, 2008b. ISSN 0031-9201. doi: https://doi.org/10.1016/j.pepi.2008.04.009. URL https://www.sciencedirect.com/science/article/pii/S0031920108000794. Frontiers and Grand Challenges in Mineral Physics of the Deep Mantle.

Yoshino, T., Matsuzaki, T., Shatskiy, A., and Katsura, T. The effect of water on the electrical conductivity of olivine aggregates and its implications for the electrical structure of the upper mantle. *Earth and Planetary Science Letters*, 288(1):291–300, 2009. ISSN 0012-821X. doi: https://doi.org/10.1016/j.epsl.2009.09.032. URL https://www.sciencedirect.com/science/article/pii/S0012821X09005664.

Yoshino, T., Ito, E., Katsura, T., Yamazaki, D., Shan, S., Guo, X., Nishi, M., Higo, Y., and Funakoshi, K.-i. Effect of iron content on electrical conductivity of ferropericlase with implications for the spin transition pressure. *Journal of Geophysical Research: Solid Earth*, 116(B4), 2011. doi: https://doi.org/10.1029/2010JB007801. URL https://agupubs.onlinelibrary.wiley.com/doi/abs/10.1029/2010JB007801.

Yoshino, T., Shimojuku, A., Shan, S., Guo, X., Yamazaki, D., Ito, E., Higo, Y., and Funakoshi, K.-i. Effect of temperature, pressure and iron content on the electrical conductivity of olivine and its high-pressure polymorphs. *Journal of Geophysical Research: Solid Earth*, 117(B8), 2012. doi: https://doi.org/10.1029/2011JB008774. URL https://agupubs.onlinelibrary.wiley.com/doi/abs/10.1029/2011JB008774.

Yoshino, T., Shimojuku, A., and Li, D. Electrical conductivity of stishovite as a function of water content. *Physics of the Earth and Planetary Interiors*, 227:48–54, 2014. ISSN 0031-9201. doi: https://doi.org/10.1016/j.pepi.2013.12.003. URL https://www.sciencedirect.com/science/article/pii/S0031920113001945.

Yousheng, X., Catherine, M., and Brent T., P. The effect of alumina on the electrical conductivity of silicate perovskite. *Science*, 282(5390):922 – 924, 1998. ISSN 00368075. URL https://search.ebscohost.com/login.aspx?authtype=shib&custid=s1240919&profile=eds.

Zhang, B., Yoshino, T., Wu, X., Matsuzaki, T., Shan, S., and Katsura, T. Electrical conductivity of enstatite as a function of water content: Implications for the electrical structure in the upper mantle. *Earth and Planetary Science Letters*, 357-358:11–20, 2012. ISSN 0012-821X. doi: https://doi.org/10.1016/j.epsl.2012.09.020. URL https://www.sciencedirect.com/science/article/pii/S0012821X1200516X.

Šachl, L., Velímský, J., Fullea, J., and Martinec, Z. Inversion of the satellite observations of the tidally induced magnetic field in terms of 3-d upper-mantle electrical conductivity: Method and synthetic tests. *Geophysical Journal International*, submitted.

List of Figures

List of Tables